

Migration Behavior of Tungsten Carbide in the Dissimilar Joints of WC-TiC-Ni/304 Stainless Steel Using Robotic MIG Welding



Guotao Ying, Hongying Gong and Peiquan Xu

Abstract Using robotic metal inert gas (MIG) welding, WC-TiC-Ni/304 stainless steel was fabricated using pure nickel as welding wire. The welds consisted of the austenitic γ -Ni matrix, dissolved WC, and compound carbide (W, M)C. Electromagnetic stirring-induced (type I), diffusion-induced (type II), and shear-induced (type III) WC migration led to WC_a and WC_b type migration. The gradient layer and η -phase were formed at the interface. WC_a migration (type I and type II) showed that arc plasma provided enough energy for WC_a long-range migration from the heat affected zone (HAZ) to the fusion zone. WC_b migration (III) exhibited the stress levels to be above the yield stress in the fusion zone. A self-sealing model was put forward to describe WC migration and the formation of gradient layers. The results showed that WC migration not only occurred in the fusion zone, but also in the HAZ, especially near the top surface, which led to gradient layer, η phase and tungsten dissolution-re-precipitation on the surface of WC. The results also indicated that the fusion zone had the ability to cure the cracks itself during the robotic MIG welding.

Keywords Robotic MIG welding · Electromagnet-induced migration · Diffusion-induced migration · Shear-induced migration · Gradient layer

1 Introduction

Among ceramics, carbides of transition metals such as WC, TiC or TaC are refractory compounds and possess high hardness and strength, which are maintained even at elevated temperatures [1]. Especially WC-based cermet has been widely used in military, aerospace, automotive, marine, petrochemical, mining, electronics, microelectronics and wood industries [2] since decades in various

G. Ying · H. Gong · P. Xu (✉)
College of Materials Engineering, Shanghai University of Engineering Science,
Shanghai 201620, China
e-mail: ppxu@sues.edu.cn

engineering applications, such as pipe-valve component, cutting tools, drill tips and as well as various wear-resistance parts [3–5]. However, WC dissolution phenomenon usually happened during liquid phase sintering of WC-Co alloys, fusion welding of WC-Co/ steel or WC laser clad. During the dissolution, the alloys, welds or clad always display a skeleton of WC grains embedded in a Co/Fe rich matrix [6] and then the structures loss the original densification. In addition, WC dissolution varies with temperature and forces: brim dissolution; transcrystalline rupture; aggregate coarsening; large region yield; carbon or tungsten diffusion from inner of WC to WC/ β interface; iron diffusion from matrix to WC [7–10], which deteriorates the original microstructure and mechanical properties. Welding is accepted for joining cemented carbide for simple applications, and likewise for those involving the most complicated critical structures where failure could be destructive to life and property. The welded joint is designed to meet a certain combination of properties required by the end use. Thus, the resulting mechanistic understanding of WC dissolution will be used to improve the weldability of cemented carbide during dissimilar welding of cemented carbide and steel and provide a scientific basis for cemented carbide-steel application in “next generation” oil and gas transportation equipment under conditions of technological importance.

Most of the important, nano-WC based cermet is under development to solve the problem of the low lifetime of cermet product because of the beneficial effect of the size and the shape of WC crystals on the mechanical properties [2, 11–13]. Nano-WC is the most reactive one, higher specific surface areas enhance welding activity and recrystallization process of WC grains, therefore, the extensive growth and dissolution of WC nano-grains easily occur during welding.

Besides WC dissolution in liquid Co/Fe matrix, element diffusion also leads to WC dissolution in solid phases accompanied by liquid dissolution [14–19]. In generally, mechanical alloying is a solid state processing technique involving repeated welding, fracturing, and rewelding of powder in high energy ball mill [20, 21], which is a good choice to investigate WC dissolution in the solid W-Fe-C system. Many studies [15, 18, 22, 23] also revealed that the element additives had a strong effect on the WC dissolution in solid phases during element diffusion. These additives included carbon, nickel, iron, rare earth, chromium, and something else. The main role of RE additives was addressed during sintering when their presence at the boundary of WC induced oxide dispersion strengthened effectiveness and inhibition of recrystallization process of WC grains [11, 24]. It was also concluded that an effective control of the reaction can be achieved by increasing in the binder composition the ratio between the elements without affinity and those with affinity to carbon and/or enlarging the carbon content [25]. Thus, the size of WC crystals had a strong effect on the mechanical properties of WC/Co. Research results [13, 14] also indicated that mechanical properties were influenced by the shape of WC crystals.

The present research aims to investigate WC migration during robotic MIG welding. Consequently, WC migration through transition layer based on thermo-dynamics and WC migration in the liquid W-M-C system are discussed.

2 Experimental

WC-TiC-Ni used in present study has a chemical composition (wt%) of 15 TiC, 79 WC, and balance Ni. Hard phases WC, TiC are embedded in the binder nickel matrix. The chemical composition (wt%) of 304 stainless steel is 0.08 carbon, 2.0 manganese, 0.045 phosphorus, 0.03 sulfur, 1.0 silicon, 18.2 chromium, 10.1 nickel, and balance iron. Nickel wire is used as filler metal and has a chemical composition (wt%) of 0.05 carbon, 0.1 manganese, 0.15 silicon, 0.1 iron, 0.1 cobalt, and 99.5 nickel, impurity does not exceed 0.5, and the diameter is 1.2 mm. The base materials were cut into plate with a square section of 200 mm × 100 mm and 4-mm thick with the 30°, 45° and 60° grooves respectively.

As shown in Fig. 1, welded joints were prepared using GLC 603 QUINTO welder with single wire, welding positioner, CLOOS@350 robot manipulator with control ROTROL II. With argon, the metal transfer mode, for the range of welding conditions investigated in present research, is normally globular transfer and there is no transition to spray transfer. The parameters for robotic MIG welding were shown in Table 1.

Heat input is a relative measure of the energy transferred per unit length of weld. It is typically calculated as the ratio of the power to the speed of the arc as follows,

$$H = (60 \cdot Q)/(1000 \cdot S) \quad (1)$$

where, H is the heat input (kJ/mm), S is the travel speed (mm/min), and the rate of heat transfer Q from the arc to the workpiece is determined by the following equation [26],

$$Q = \eta \cdot Q_{nominal} \quad (2)$$

where η is arc efficiency, here, η is equal to 0.8, $Q_{nominal}$ is the nominal power of the arc, $Q_{nominal} = E \cdot I$, where E is arc voltage, I is welding current. With GLC 603 QUINTO welder, E values are set before welding, and pick I values from the indicator.

Fig. 1 Architecture of robotic MIG welding of cemented carbide to 304 stainless steel

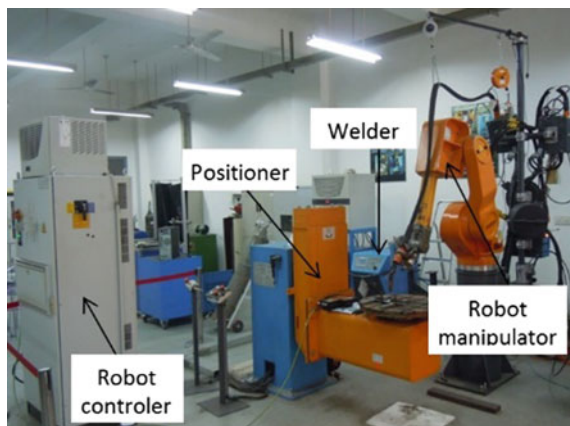


Table 1 Robotic MIG welding parameters and weld defects in present study

d (mm)	No.	Heat input (J/mm)	Groove (°)	Max. d_1 (mm)	Weld defects	Crack
4	A1	321	30	42.98	Cracks	30 s after welding
	A2	406	30	56.94	Cracks	5 s after welding
	A3	463	30	136.94	Cracks	2 min after welding
	A4	417	30	103.39	–	–
	A5	411	30	95.77	–	–
6	I-1	418 (416)	30	143.05	Spatter, porosity	No cracks (2 s)
	I-2	429	30		Insufficient	10 s after welding
	I-3	392	30		Insufficient	5 s after welding
	II-1	432 (367)	45	120.8	Insufficient	No cracks (instant)
	II-2	439 (459)	45		Insufficient	No cracks (instant)
	II-3	420 (363,377)	45		–	No cracks (instant)
	III-1	529	60	186.68	Burn-through	During weld
	III-2	566 (517)	60		EP	During weld
	III-3	441	60		Insufficient	6 h after welding

Tungsten carbide is hexagonal with lattice constants $a = 2.91 \text{ \AA}$ and $c = 2.84 \text{ \AA}$. If sufficient C and W dissolved into the Co, the phase is stabilized [27]. The microstructure was characterized by optical metallography (OM), electro-probe micro analyzer (EPMA) and scanning electron microscopy (SEM). SEM images were performed using S-4800 (Hitachi, Japan). The specimens were prepared by the standard metallographic procedures and etched with the Murakami's reagent [28]. The reagent ferric chloride (3 g FeCl_3 and 100 ml H_2O) was used for nickel binder removal (10 s).

3 Results

3.1 Weld Formation

For metallographic examination, the specimens were cut vertical to welded seam. After grounded, polished and etched, the specimens were then investigated along the position of cross-section. Figure 2 illustrated the influence of thickness and heat

input on the weld appearance of WC-TiC-Ni/304 joint. The result (Table 1) indicated the use of higher heat input (A3: 463 J/mm) led to wider fusion zone compared to lower heat input (A1: 321 J/mm; A2: 406 J/mm). Cracks were observed through the depth in specimen A1 and A2 at a minimum of 20, 5 s after welding. The cracks occurred at lower temperature, initiated from the HAZ near cemented carbide at the start and then propagated to cemented carbide. The average length of longitudinal cracks was 43 and 49 mm, and the average length of transverse cracks was 12 and 11 mm respectively. When the use of medium heat input (A4: 417 J/mm, A5: 411 J/mm), the consequent residual stress could not meet the requirement of crack initiation and propagation, cracks were not observed in specimens A4 and A5. However, with heat input H increased continuously (A3: 463 J/mm), the cracks occurred. Close to the top surface of welded joint, the welds were sensitive to transverse cracking. With the increase of heat input, more transverse cracks appear to occur on the surface of the bead. The cold cracks, when it happened, always occurred in the HAZ near cemented carbide; however, the hot cracks, when it happened, always occurred in the welds, on the top surface of previous bead, and then they propagated in transverse direction.

When 6-mm thick base materials were used, the cracks were always observed on the WC-TiC-Ni side. With the increase of groove angle, more and more filler metals were needed to fill the groove, the cracking susceptibility increased accordingly. When groove angle was equal to 30° , spatter, porosity or insufficient penetration were easily observed. Especially, two layers were adopted, no cracks occurred when $P = 418$ J/mm for first layer, however, cracks were propagated just after welding. When groove increased to 45° , two layers could not meet the requirement of weld penetration. When three layers were adopted, excess penetration (EP) made the weldment fail. EP, even burn through occurred when heat input increased to 500 or three layers were selected for groove angle 60° .

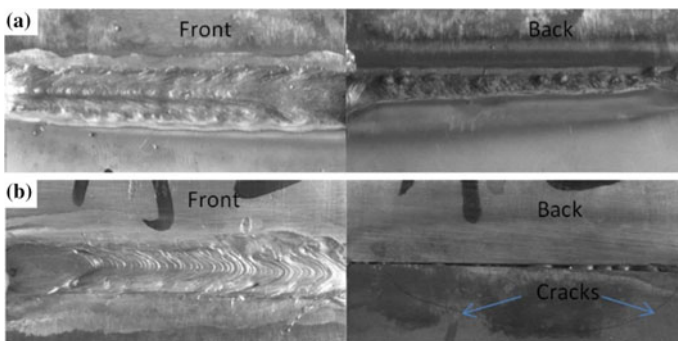


Fig. 2 Comparison of weld appearance between a $d = 4$ mm and b $d = 6$ mm (left: front; right: back)

3.2 Microstructures

For further investigation, the transverse cross-sections of 4 and 6-mm thick specimens were conducted in Figs. 3, 4 and 5. Cross-sectional view of typical joint A1 was illustrated in Fig. 3. WC migration and grain growth: normal grain growth (NGG), abnormal grain growth (AGG) were observed near WC-TiC-Ni/welds interface in both 4 and 6-mm thick specimens. In current research, an abnormal grain was defined to be around seven times larger than the average grain size [29]. The WC migration from cemented carbide to weld, region 'A' in Fig. 3, was amplified in Fig. 4a. The distance from original location to current position was nearly 200 μm .

The WC migration, always accompanied by grain growth, occurred near the top surface because of larger heat input and forces during welding. Especially, they were affected by weld pool mixed with strong convection currents resulting from the interaction between the electromagnetic and Marangoni forces. Far from 304/fusion zone interface, equiaxed austenite grains and annealing twins were observed (Fig. 5c), however, the weld was embrittled by $\alpha(\delta)$ ferrite \rightarrow σ phase at 820 $^{\circ}\text{C}$ or $\alpha(\delta)$ ferrite \rightarrow α ferrite with low chromium (Fig. 5d) in HAZ at 304 stainless steel side. Gradient microstructure in heat affected zone was observed not only in 4-mm thickness specimens (Fig. 4c) but in 6-mm thickness specimens (Fig. 5a). Coarse WC grains and fine dispersive WC grains were observed in both weld and HAZ near WC-TiC-Ni/Ni interface. Coarse WC grains were divided into two parts (Fig. 4d): NGG and AGG, which were also observed in 6-mm thick specimens (Fig. 5e).

NGG was owed to the WC nucleation and grain growth in liquid nickel during welding or final solidification stage; however, AGG was an abrupt growth phenomenon at elevated temperature and WC grains had a strong tendency for AGG because of the difference of growth rate for different nucleation of growth ledges, mass transfer across the interface and long range diffusion. Both grain growth

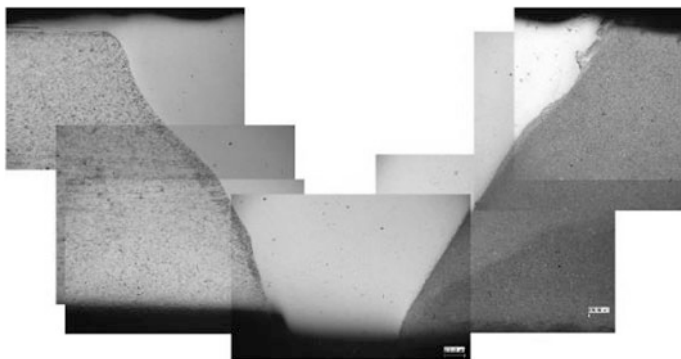


Fig. 3 Cross-sectional view of a typical joint (A1) of 304 stainless steel (left side) and WC-TiC-Ni (right side) with pure nickel welding wire ($d = 4$ mm)

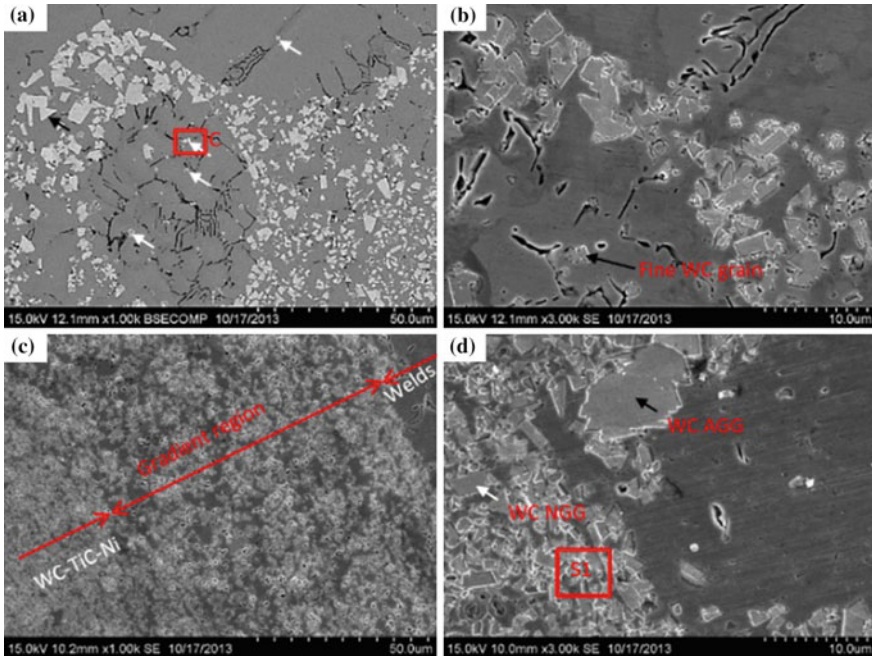


Fig. 4 WC behaviors near WC–TiC–Ni/weld interface in 4-mm thick specimens. **a** Migration of WC grains from cemented carbide to weld in specimen A1 (region ‘A’ in Fig. 3), white arrow showing fine WC grains; black arrow showing coarse WC grains; **b** WC phase surrounded by nickel from both binder and filler metal (region ‘C’ in a); **c** Gradient microstructure in specimen A5; **d** WC NGG and WC AGG observed in specimen A4

behaviors were strongly influenced by the initial size distribution [29, 30]. By contrast, 6-mm thick specimens had much stronger tendency for WC migration and grain growth than 4-mm thick specimens.

3.3 Morphology and Compositions

SEM images of the fusion zone and WC–TiC–Ni/welds interface were illustrated in Fig. 6, taken near the center of the cross section of the weldment. Figure 6a illustrated SEM images of WC–TiC–Ni/welds interface in specimen A1, white arrows showing grain boundaries, and black arrows showing the nickel grains. The morphology was characterized using backscattered electron imaging and secondary electron imaging respectively. The spectrums used for composition analysis were marked with yellow cross or yellow rectangular. And the corresponding composition and EDS spectrum were listed in Table 2. Dissolved WC embedded in nickel matrix, nickel mixtures of original nickel in WC–TiC–Ni and nickel from the filler

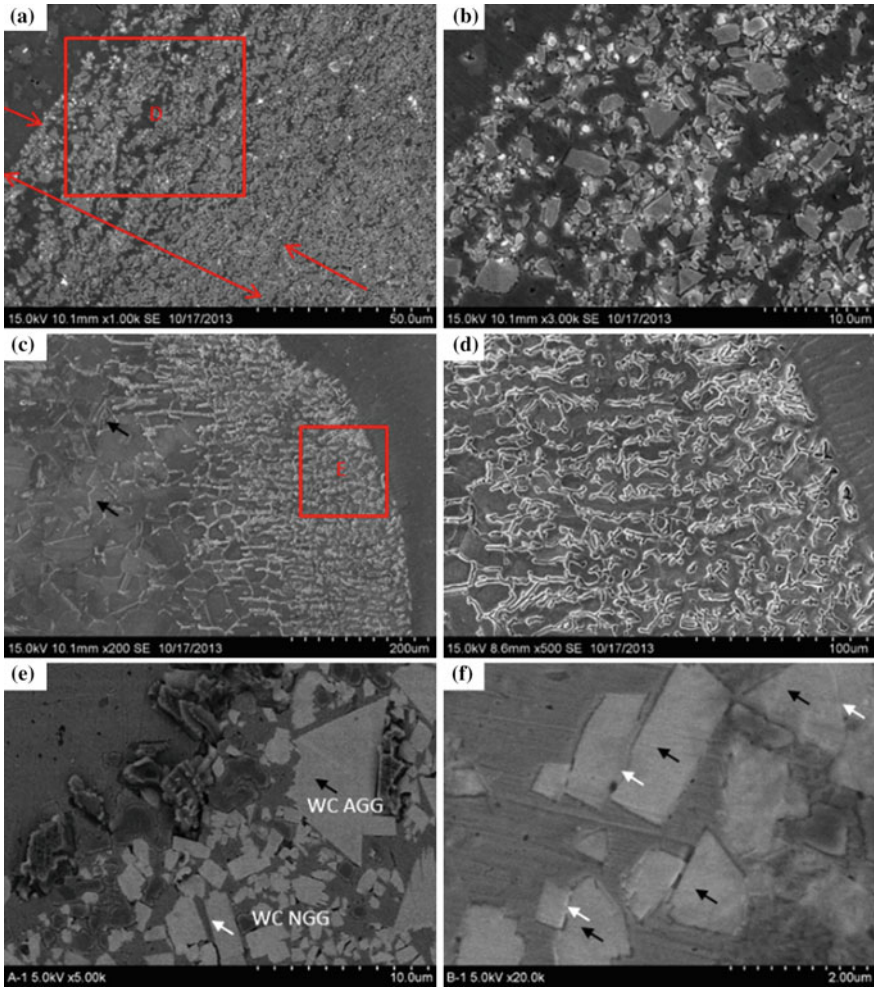


Fig. 5 SEM image showing the WC behaviors in 6-mm thick specimens. **a** Gradient microstructure in I-2 specimen; **b** Gradient WC-TiC-Ni accompanied by grain growth (region 'D' in **a**); **c** (Fe, Cr)/Ni solution near steel side in specimen I-2, black arrows indicate the original equiaxed austenite grains and annealing twins; **d** High magnification of region 'E' in **c**. **e** WC abnormal grain growth observed in specimen I-2; black arrow indicates AGG WC, white arrow indicates NGG WC. **f** WC migration to weld in specimen II-2; black arrows indicate the dissolved WC grains; white arrows show the interface WC/WC

metal. The grain size of nickel in welds was larger than that in HAZ near WC-TiC-Ni/welds interface. The dissolved WC indicated blunt corner. And the sharp triangle WC or rectangular WC grains were not observed. Results on composition analysis of WC-TiC-Ni/welds manifested that “pro-dissolved carbide” (SP1) had the average content (wt%) 16.22W, 43.61Ni, 21.52Fe, 1.22C, 9.45Ti and

5.36%Cr characterized with tungsten depletion. In contrast to weld, the WC and TiC were surrounded by nickel and iron liquid. The “pro-dissolved carbide” meant WC dissolution in nickel matrix was a gradual process until WC disappeared in the matrix completely.

However, it was difficult for pro-dissolved WC to transit from WC → η phase (Fe_3W_3C or Fe_6W_6C), the driving force for growth of “pro-dissolved carbide” grain was not enough, which made it impossible for nickel or iron atoms substitute for tungsten atoms. Therefore, WC → η phase transition was inhibited. Figure 6b

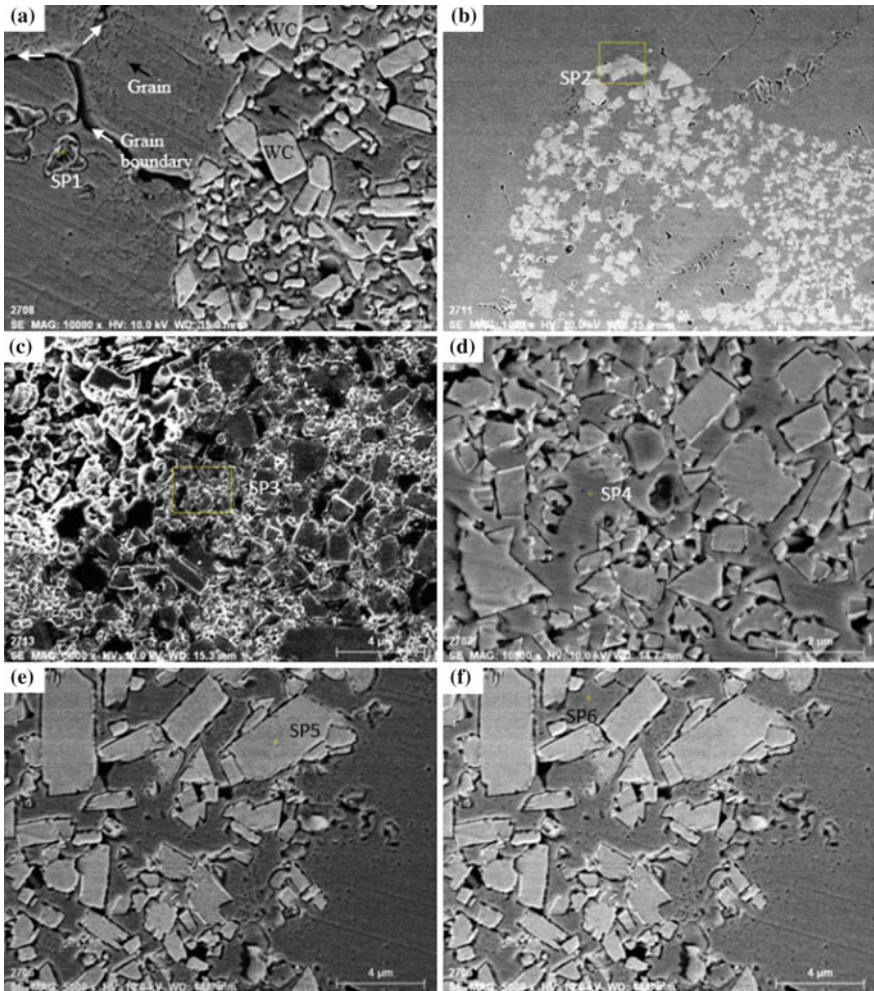


Fig. 6 SEM image showing the WC dissolution in 4-mm thick specimens, **a** SP1 in specimen A1, white arrow showing grain boundary; black arrows showing the nickel matrix; **b** SP2 in specimen A1; **c** SP3 in specimen A4; **d** SP4 in specimen A5; **e** SP5 in specimen A5; **f** SP6 in specimen A5

showed another WC dissolution in non-equilibrium η phase layer, was near the fusion line “non-equilibrium η phase” (SP2) had the average content (wt%) 40.50W, 44.71Ni, 12.91Fe, 1.87C characterized with carbon depletion. WC \rightarrow η phase transition occurred and $\text{Fe}_3\text{W}_3\text{C}$ compound was observed. This meant WC had experienced a non-equilibrium transition from stable WC to equilibrium η phase, however, the period of the welding was very short and volatilization, if any, can occur mostly from the surface region. So the carbides were non-equilibrium phases. At the HAZ near WC-TiC-Ni/welds interface, carbon depletion phenomenon was observed and distributed widely. The average content (wt%) of SP3 (Fig. 6c) was 72.34W, 22.06Ni, and 3.68C, characterized with carbon depletion. Because the average contents of Ni and W in M_6C and M_{12}C (M stands for Fe, Ni or Co) were nearly 23.2 and 75.30% respectively, η phase belonged to such compound carbides as M_6C and M_{12}C . In addition, W dissolution in Ni matrix (SP4 in Fig. 6d) was observed. The average contents (wt%) of SP4 were 9.34W, 64.27Ni, and 26.39Fe with carbon depletion. This meant the WC dissolution was going on accompanied by tungsten carbides decomposition into tungsten and carbon. The dissolution led to WC grains loss. Figure 6e, f showed the morphology of WC AGG. The average contents (wt%) of carbide (SP5, shown in Fig. 6e) and matrix (SP6, shown in Fig. 6f) were 94.32W, 5.68C and 16.11W, 18.40Fe, 56.88 Ni, 1.36C, 7.24Ti, which were characterized with carbon depletion.

3.4 Element Diffusion

Figure 7 showed the interfacial microstructure of specimens A1, A4, and A5 with EDS maps of as-welded joints. In the specimens A1, A4, and A5, the initial microstructures of cemented carbide (triangular, rectangular WC grains embedded in nickel binder) begin to dissolve to the fusion zone. WC dissolved in nickel with shape variation from triangular or rectangular to rounded WC grains accompanied by grain growth, which decreased the density of cemented carbide. Similar to the welded joint between cemented carbide and the steel, the microstructures of austenite and ferrite were the primary phases in HAZ and extended deeply into the steel. In the WC-TiC-Ni/welds interface, the HAZ consisted of austenite, γ -phase, η -phase, non-equilibrium carbide and WC. The fine dissolving WC grains were around the large WC grains. Vice versa, there were much more fine grains around the AGG WC grains due to the sacrifice of fine WC grains during WC dissolution and grain growth. The most notable features were undesirable voids and micro-cracking in the η phase reaction layer. The size of the voids and interfacial reaction layer were similar for all specimens. Such voids would act as origin of failure thus reducing mechanical robustness. These voids were due to the consequence of differential hot shrinkage induced by welding residual stress. WC AGG phenomenon occurred at interface in specimens A1 and A4 (Fig. 7b). However, in specimen A5 (Fig. 7c) there are less AGG WC grains. During robotic MIG welding, because the temperatures were too low to melt the WC grains, WC grains

Table 2 Composition distribution of WC behavior [wt% (at.%)]

Element	W M	Ni L	C K	Fe K	Ti K	Cr K
SP1	16.22 (4.95)	43.61 (41.68)	1.22 (5.69)	21.52(21.61)	9.45 (11.08)	5.36 (5.78)
SP2	40.50 (16.09)	44.71 (55.63)	1.87 (11.39)	12.91(16.89)	–	–
SP3	72.34 (32.91)	22.06 (31.44)	3.68 (25.61)	–	–	–
SP4	9.34 (3.14)	64.27 (67.66)	–	26.39(29.20)	–	–
SP5	94.32 (53.17)	–	5.68 (46.83)	–	–	–
SP6	16.11 (5.31)	56.88 (58.72)	1.36 (6.84)	18.40 (19.97)	7.24 (9.16)	–

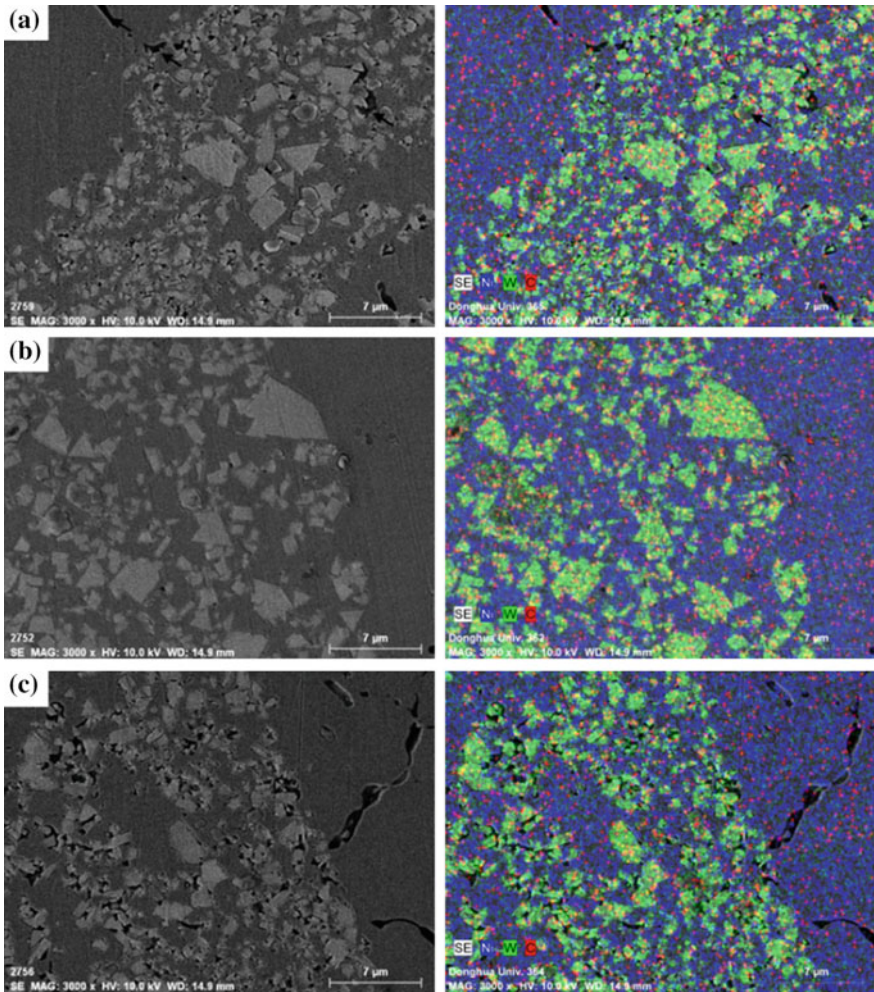


Fig. 7 SEM image and corresponding interfacial EDS compositional maps for area scanning micrograph of etched as-welded WC-TiC-Ni/304 stainless steel interface of specimens **a** A1; **b** A4; and **c** A5 (left: SEM image; right: EDS maps)

were not melted. However, under the effect of such forces as intrinsic stress, surface tension, buoyancy force, stirring behavior, and shock waves at the backside of weld pool, WC dissolution happened starting from the WC brims.

4 Discussion

4.1 Effect of Heat Input on the WC Migration

“Self-healing” model was put forward to reveal the mechanism of WC migration in welds. Figure 8a shows the schematic illustration of thermal process in an idealized vertical droplet, wire, and weld pool in WC-TiC-Ni. MIG welding melted and joined WC-TiC-Ni cemented carbide by heating them with an arc established between a continuously fed nickel wire and WC-TiC-Ni cemented carbide. The molten metals at the nickel wire tip were transferred to the weld pool by globular transfer mode across the arc gap under the effect of gravity. As shown in Fig. 8b, WC migration indicated a-type tungsten carbide (WC_a) migration in welds and b-type tungsten carbide (WC_b) migration in HAZ. WC_a grains had an uneven grain distribution; some WC_a grains were much larger than NGG WC grains, however, sizes of other WC_a grains were much smaller. There existed a dynamic equilibrium system consisted of fine WC_a grains, coarse WC_a grains, and liquid nickel matrix. On one side, fine WC grains dissolved to liquid nickel until it disappeared; on the other hand, WC nucleated at the surface of coarse WC grains at liquid/liquid or vapor/liquid interface at elevated temperature (shown as Figs. 5 and 6). WC_a featured with long-range moving with grain growth and interface I formation and interface II formation. The nickel appeared in HAZ came from both filler metal and base metal.

Heat input energy could be transferred to droplet and arc plasma, and then was transferred to workpiece. In the proposed model, energy loss q_l during robotic MIG welding: heat losses occur via conduction in the solid rod q_k and conduction in the workpiece q_w , radiation exchange with the environment q_r , convection to the shielding gas q_c , and other losses. So it can be expressed as,

$$q_l = q_r + q_c + q_k + q_w + \Delta q = (1 - \omega) \cdot Q \quad (3)$$

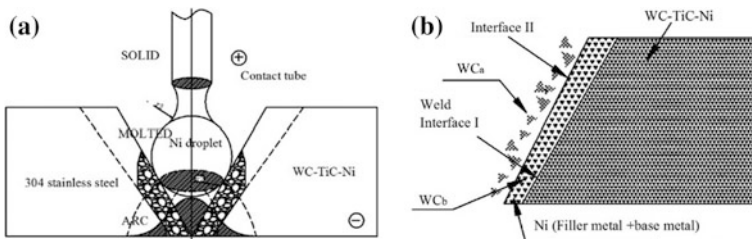


Fig. 8 Schematic illustration of **a** thermal process in an idealized vertical droplet, wire, and weld pool in WC-TiC-Ni; **b** Migration happened at heat affected zone

First, the governing thermal energy equation for energy transfer between nickel wire and droplet in cylindrical coordinates can be described as follows [31],

$$\frac{\partial \rho l}{\partial t} + \rho u \frac{\partial H}{\partial x} + \rho v \frac{\partial H}{\partial r} = \frac{\partial}{\partial x} \left(kr \frac{\partial T}{\partial x} \right) + \frac{1}{r} \frac{\partial}{\partial r} \left(kr \frac{\partial T}{\partial r} \right) + q_G''' \quad (4)$$

where ρ is the density, radial velocity v , axial velocity u , and the dependent variables are the enthalpy (H) and the specific internal thermal energy (l). r is radial distance; r_0 is outside radius; r_1 is the solid wire radius = 1.2 mm; k is thermo conductivity; x is axial distance; volumetric thermal energy generation rate q_G''' . Assume that steady motion of the solid wire, v is equal to zero, and u is equal to wire feed speed v_w . The heat transfer between nickel wire and droplet can be expressed as [31],

$$\frac{\partial \rho l}{\partial t} + \rho v_w u \frac{\partial H}{\partial x} = \frac{\partial}{\partial x} \left(kr \frac{\partial T}{\partial x} \right) + \frac{1}{r} \frac{\partial}{\partial r} \left(kr \frac{\partial T}{\partial r} \right) + q_G''' \quad (5)$$

Second, energy transfer between plasma arc (droplet) and weld pool can be expressed as follows,

$$q = \frac{\partial}{\partial t} (\rho H) + \nabla \cdot (\rho V H) \quad (6)$$

where, q is the total energy, in two or more dimensions we must use ∇ . Continuum density, specific heat, thermal conductivity, solid mass fraction, liquid mass fraction, velocity, and enthalpy are defined as follows:

$$H = h_s f_s + h_l f_l \quad (7)$$

where f_s and f_l are the mass fracture of solid and liquid; h_s and h_l are the enthalpy of solid and liquid. The direction of flow due to thermo capillary convection depends on whether the surface tension increases or decreases with temperature. In a sense, a region with higher stress σ pulls fluid from regions with lower stress σ . In addition, because the obvious difference of physical properties between WC-TiC-Ni cemented carbide and 304 stainless steel, the melting zone where warming liquid dropping toward will be determined by the above factors. In addition, the thermo capillary (Marangoni) has a significant effect on thermo-fluid-mechanics of weld pools. Surface tension generally depends on temperature, composition and electrical potential. The direction of flow due to thermo capillary convection depends on whether the surface tension increases or decreases with temperature.

In current research, the width of HAZ dH was used to estimate the WCb migration. This zone was adjacent to the welds and was not melted itself but was structurally changed because of the couple effect of thermal-mechanics. As shown in Fig. 9a, HAZ again was divided into two parts, the larger part neighboring the fusion zone containing nickel austenite, which was a quasi-equilibrium process in

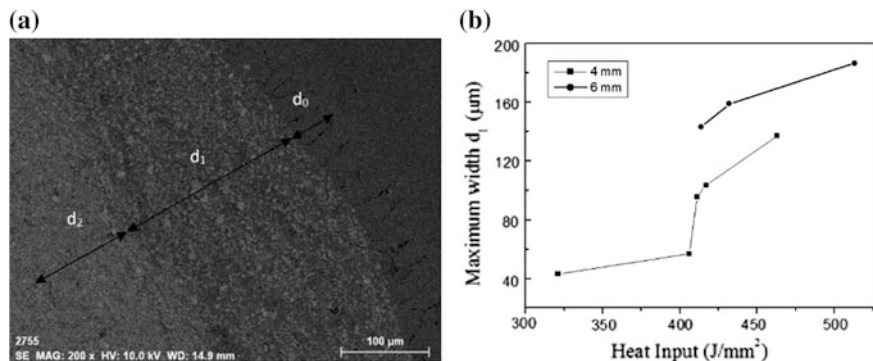


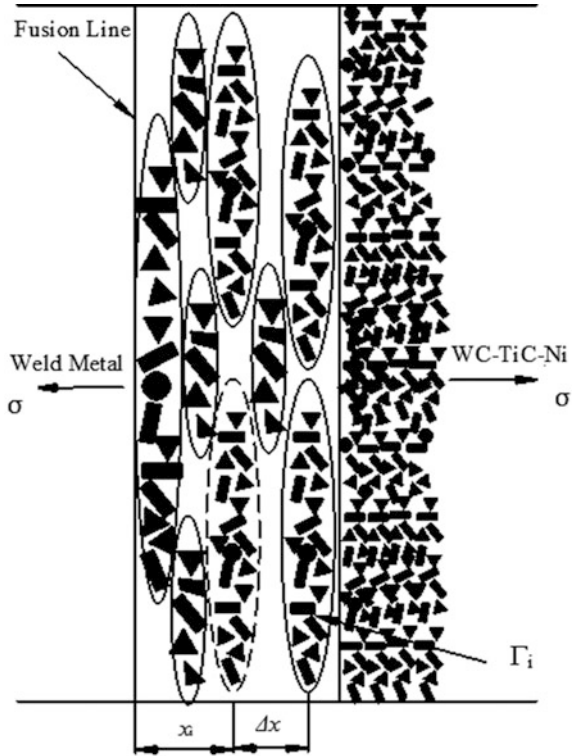
Fig. 9 **a** The definition of d_0 -width of η phase layer; d_1 -width of sparse layer; d_2 -width of diffusion zone; **b** The relationship of d_1 and heat input H

liquid nickel during welding and dominated by dissolution. The width of this part was defined as d_1 along the vertical direction, which was related to the power density of heat source. The other part neighboring the WC-TiC-Ni cemented carbide and its width was defined as d_2 along the vertical direction. d_1 and d_2 were dependent variables and determined by the thermo-mechanics coupled. Figure 9b represented the results of relationship between d_0 , d_1 , d_2 and heat input during MIG welding of 4 and 6-mm thick specimens. Because the HAZ width was estimated from the process interaction time and the thermal diffusivity of the material [27], at levels above approximately $104 \text{ W}/\text{cm}^2$, the HAZ width became roughly constant. This was due to the fact that the HAZ grew during the heating stage at power densities that were below $104 \text{ W}/\text{cm}^2$, but at higher power densities it grew during the cooling cycle. Thus, at low power densities, the HAZ width was controlled by the interaction time, whereas at high power densities, the width was independent of the heat source interaction time.

WC_a migration occurred in the region between HAZ and fusion zone. WC grains in weld pool reacted with the nickel from the melting filler rod, η phases were formed when nickel atoms substituted some tungsten atoms with carbon depletion. Too high carbon content led to the formation of graphite and too low carbon content led to the formation of an additional carbide, η phases (M_6C or M_{12}C) in quasi-equivalent state or transition carbide in non-equivalent [29, 30]. The difference in the possible loss of the carbon and tungsten due to volatilization must also be inconsiderable because the time period of the MIG welding was very short and volatilization, if any, could occur mostly from the surface region. During heating, among solid nickel wire and cemented carbide, molten droplet and weld pool, and arc plasma, droplet or arc plasma dominated the WC migration. Therefore, WC behavior included η layer formation; decomposition of $\text{WC} \rightarrow \text{W} + \text{C}$, normal grain growth, and abnormal grain growth during WC_a migration.

As described schematically in Fig. 10 for an idealized migrated WC, possible thermal processes that may interact with the forces on cemented carbide to cause WC_b migration. For the i th ideal plane Γ_i in HAZ where WC migration occurred, its

Fig. 10 The stress applied on the idealized migrated WC and its failure mechanism



area is S ; Δx_i and x are the distance of WC grains migration from its current position and from fusion line respectively. So the volume of WC in Γ_i is $S \cdot \Delta x_i \cdot f_{WC}$; σ is the total stress applied on the Γ_i containing migrated WC; σ_s is the yield strength. The energy for WC detachment from the original counterpart is $q_0(x)$, and the energy for WC migration per displacement is $q_m(x)$, so,

$$q_{WC} = S \cdot \Delta x \cdot f_{WC} \cdot q_m(x) + q_0(x) \tag{8}$$

Therefore,

$$\left\{ \begin{aligned} \frac{\partial}{\partial x} (kr \frac{\partial T}{\partial x}) + \frac{1}{r} \frac{\partial}{\partial r} (kr \frac{\partial T}{\partial r}) + q_G''' = \frac{\partial}{\partial t} (\rho H) + \nabla \cdot (\rho V H) = q_{WC} + Q \\ \sigma \geq \sigma_s \end{aligned} \right. \tag{9}$$

Criteria: assuming the number of WC grains is n in unit area, energy consumption for migration of per WC grain (WC_b) is $q_m(x)$ in unit distance along vertical direction. From the view of energy consumption, if energy provided by arc is greater or equal to the energy requirement for WC migration, that is, $q \geq q_{WC} + Q$, WC migration happens. In other words, when $\sigma \geq \sigma_s$, WC migration happens. When WC_b occurs at elevated temperature, liquid nickel can

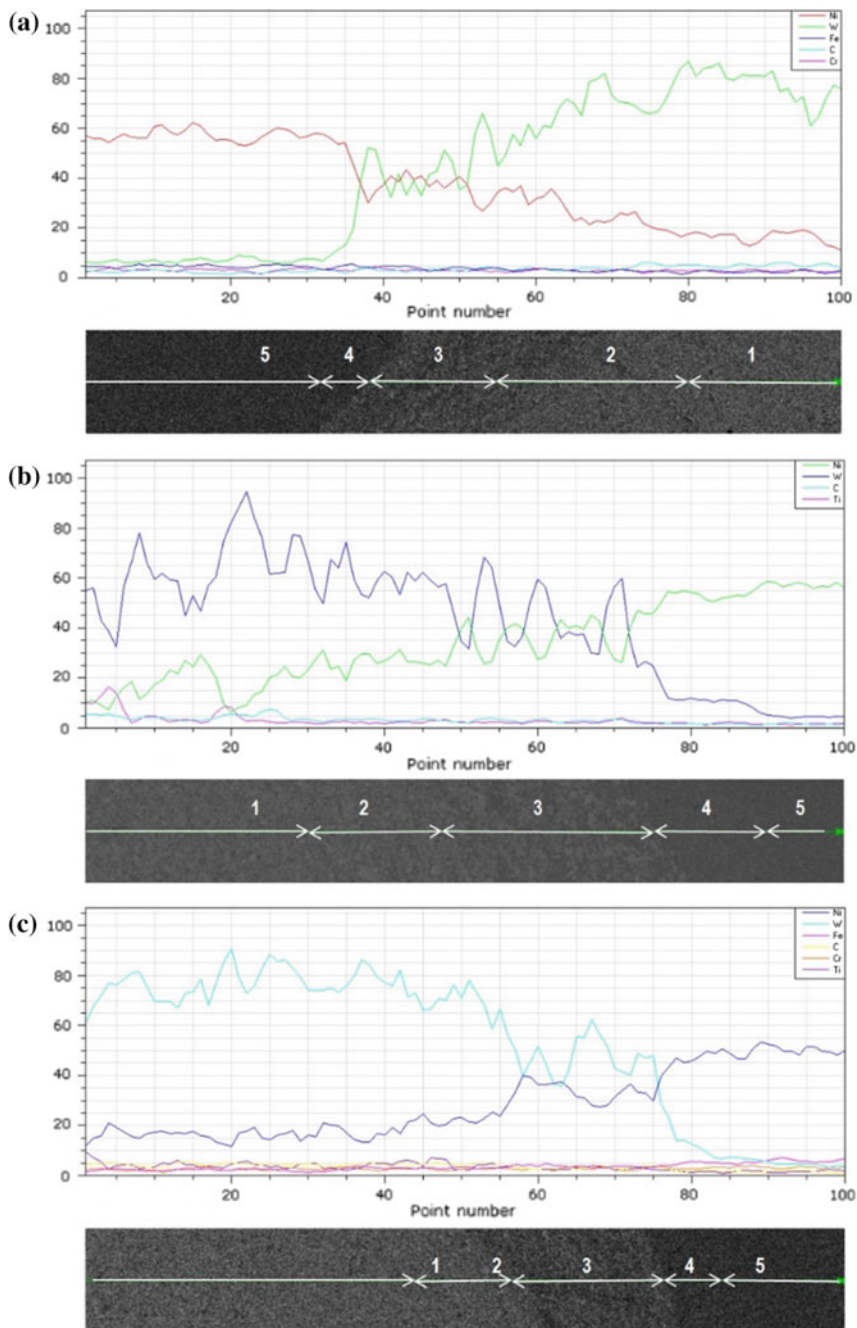


Fig. 11 Elements distribution at WC-TiC-Ni/Ni interface of specimens **a** A1; **b** A2, and **c** A5 (1. WC-TiC-Ni base metal; 2. HAZ; 3. Gradient layer; 4. η phase layer; 5. the fusion zone)

cure the cracks formation during welding. And the nearer to fusion line, the longer distance WC migrated.

According to elements distribution in the WC-TiC-Ni/welds interface, as shown in Fig. 11, approximate equilibriums were observed in region 3 (gradient layer) of specimens A1, A4, and A5, which agreed with previous investigation. However, in region 2 and region 4, there were obvious and consecutive transitions from the position with high concentration to that with the low concentration.

4.2 Effect of Heat Intensity on the WC Migration

If WC_a grains were characterized with electromagnetic-induced migration, the electromagnetically induced motion produced a rapid rate of transport of WC from HAZ into the weld pool, the formation of dispersive distribution of fine WC grains could be explained by the mechanism of dissolution-re-precipitation. Coarse WC grains and fine dispersive WC grains dissolved to liquid nickel which led to η formation. Because HAZ grew during the heating stage at power densities below 104 W/cm² [31], WC_a grain migration was controlled by the interaction time, e.g. more WC_a migration accompanied by normal grain growth and abnormal grain growth were observed in the fusion zones, which are mainly dominated by electromagnetic stirring effect. At higher power densities it grew during the cooling cycle. At high power densities, the width is independent of the heat source interaction time. The HAZ width grew during the cooling cycle as the heat of fusion was removed from the fusion zone and was proportional to the fusion zone width.

5 Conclusion

The amount and distance of WC_a migration in the fusion zone, for a given pure nickel welding wire, was determined by electromagnetically induced motion in the weld pool. This motion produced a rapid rate of transport of WC from HAZ into the fusion zone. WC_b migration indicated the stress levels to be above the yield stress in the fusion zone on-cooling during robotic MIT welding. WC behavior included the formation of η layer, decomposition of tungsten carbide, and grain growth during WC migration.

Tungsten was observed in the fusion zone near WC-Co side due to the dissolution and chemical decomposition of tungsten carbides. In the fusion zone, gradient layer was helpful for metallurgical bonding and it had the ability to cure the cracks.

Acknowledgements This work is financially supported by the National Natural Science Foundation of China (51475282, 51105240), the “Shu Guang” Project of Shanghai Municipal Education Commission and Shanghai Education Development Foundation (13SG54).

References

1. Exner HE (1979) Physical and chemical nature of cemented carbides. *Int Met Rev* 24: 149–173
2. Sui Y, Luo H, Lv Y et al (2016) Influence of brazing technology on the microstructure and properties of YG20C cemented carbide and 16Mn steel joints. *Weld World* 60(6):1269–1275
3. Guo Y, Wang Y, Gao B et al (2016) Rapid diffusion bonding of WC-Co cemented carbide to 40Cr steel with Ni interlayer: effect of surface roughness and interlayer thickness. *Ceram Int* 42(15):16729–16737
4. Klümsner T, Wurster S, Supancic P et al (2011) Effect of specimen size on the tensile strength of WC-Co hard metal. *Acta Mater* 59(10):4244–4252
5. Mirski Z, Granat K, Stano S (2016) Possibilities of laser-beam joining cemented carbides to steel. *Weld Int* 30(3):187–191
6. Lay S, Dennadieu P, Loubradou M (2010) Polarity of prismatic facets delimiting WC grains in WC-Co alloys. *Micron* 41(5):472–477
7. Ahn S, Kang S (2008) Dissolution phenomena in the Ti ($C_{0.7}N_{0.3}$)-WC-Ni system. *Int J Refract Metal Hard Mater* 26(4):340–345
8. Li LQ, Liu DJ, Chen YB et al (2009) Electron microscopy study of reaction layers between single-crystal WC particle and Ti-6Al-4V after laser melt injection. *Acta Mater* 57(12):3606–3614
9. Barbatti C, Garcia J, Liedl G et al (2007) Joining of cemented carbides to steel by laser beam welding. *Materialwiss Werkstofftech* 38(11):907–914
10. Lavergne O, Robaut F, Hodaj F et al (2002) Mechanism of solid-state dissolution of WC in Co-based solutions. *Acta Mater* 50(7):1683–1692
11. Cheniti B, Miroud D, Badji R et al (2017) Effect of brazing current on microstructure and mechanical behavior of WC-Co/AISI 1020 steel TIG brazed joint. *Int J Refract Metal Hard Mater* 64:210–218
12. Su JZ, Guo LJ, Bao NZ et al (2011) Nanostructured $WO_3/BiVO_4$ heterojunction films for efficient photo electro-chemical water splitting. *Nano Lett* 11(5):1928–1933
13. Zou J, Sun SK, Zhang GJ et al (2011) Chemical reactions, anisotropic grain growth and sintering mechanisms of self-reinforced ZrB_2 -SiC doped with WC. *J Am Ceram Soc* 94(5):1575–1583
14. Guo J, Fang ZZ, Fan P et al (2011) Kinetics of the formation of metal binder gradient in WC-Co by carbon diffusion induced liquid migration. *Acta Mater* 59(11):4719–4731
15. Zhang XZ, Liu GW, Tao JN et al (2017) Vacuum brazing of WC-8Co cemented carbides to carbon steel using pure Cu and Ag-28Cu as filler metal. *J Mater Eng Perform* 26(2):488–494
16. Niu L, Hojamberdiev M, Xu YH (2010) Preparation of in situ-formed WC/Fe composite on gray cast iron substrate by a centrifugal casting process. *J Mater Process Tech* 210(14): 1986–1990
17. Konyashin I, Hlawatschek S, Ries B et al (2009) On the mechanism of WC coarsening in WC-Co hard metals with various carbon contents. *Int J Refract Metal Hard Mater* 27(2): 234–243
18. Upadhyaya GS (1998) *Cemented tungsten carbides: production, properties, and testing*. Noyes Publications, Westwood
19. Fernandes CM, Senos AMR, Vieira MT (2007) Control of η carbide formation in tungsten carbide powders sputter-coated with (Fe/Ni/Cr). *Int J Refract Metal Hard Mater* 25(4): 310–317
20. Mercado WB, Cuevas J, Castro IY et al (2007) Synthesis and characterization of Fe_6W_6C by mechanical alloying. *Hyperfine Interact* 175(1–3):49–54
21. Suryanarayana C (2001) Mechanical alloying and milling. *Prog Mater Sci* 46(1–2):1–184
22. Wang Y, Zhu N, Wang H et al (2017) Interdiffusion and diffusion mobility for fcc Ni-Co-Al alloys. *Metall Mater Trans A* 48(3):943–947

23. Weidow J, Johansson S, Andrén HO et al (2011) Transition metal solubilities in WC in cemented carbide materials. *J Am Ceram Soc* 94(2):605–610
24. Liu S, Huang Z, Liu G et al (2006) Preparing nano-crystalline rare earth doped WC/Co powder by high energy ball milling. *Int J Refract Metal Hard Mater* 24(6):461–464
25. Rios O, Cupid DM, Seifert HJ et al (2009) Characterization of the invariant reaction involving the L, η , γ and σ phases in the Ti–Al–Nb system. *Acta Mater* 57(20):6243–6250
26. Kou S (2002) *Welding metallurgy*, 2nd edn. Wiley, Hoboken, pp 205–418
27. Kim CS, Massa TR, Rohrer GS (2008) Interface character distributions in WC–Co composites. *J Am Ceram Soc* 91(3):996–1001
28. ASM (2004) *ASM handbook volume 9: metallography and microstructures*. ASM International, Materials Park, OH, pp 125–249
29. Mannesson K, Jeppsson J, Borgenstam A et al (2011) Carbide grain growth in cemented carbides. *Acta Mater* 59(5):912–1923
30. Yang DY, Yoon DY, Kang SJL (2011) Suppression of abnormal grain growth in WC–Co via two-step liquid phase sintering. *J Am Ceram Soc* 94(4):1019–1024
31. Kim YS, McEligot DM, Eagar TW (1991) Analyses of electrode heat transfer in gas metal arc welding. *Weld J* 70(1):20-s–31-s